High-order-harmonic generation from inhomogeneous fields

M. F. Ciappina,[1] J. Biegert,[1,2] R. Quidant,[1,2] and M. Lewenstein[1,2]
[1]*ICFO-Institut de Ciències Fotòniques, 08860 Castelldefels (Barcelona), Spain*
[2]*ICREA-Institució Catalana de Recerca i Estudis Avançats, Lluis Companys 23, 08010 Barcelona, Spain*
(Received 7 October 2011; published 22 March 2012)

We present theoretical studies of high-order-harmonic generation (HHG) produced by nonhomogeneous fields resulting from the illumination of plasmonic nanostructures with a short laser pulse. We show that both the inhomogeneity of the local fields and the confinement of the electron movement play an important role in the HHG process and lead to the generation of even harmonics and a significantly increased cutoff, more pronounced for the longer-wavelength cases studied. In order to understand and characterize the new HHG features, we employ two different approaches: the numerical solution of the time-dependent Schrödinger equation and the semiclassical approach known as the strong-field approximation (SFA). Both approaches predict comparable results and show the new features, but by using the semiclassical arguments behind the SFA and time-frequency analysis tools, we are able to fully understand the reasons for the cutoff extension.

DOI: 10.1103/PhysRevA.85.033828 PACS number(s): 42.65.Ky, 78.67.Bf, 32.80.Rm

I. INTRODUCTION

Coherent light sources in the ultraviolet (UV) to extreme ultraviolet (XUV) spectral range are in high demand nowadays for basic research, material science, biology, and possibly lithography [1]. Their caveat is a demanding infrastructure for XUV generation and target delivery as well as its low efficiency and low duty cycle. The recent demonstration based on surface plasmon resonances as light enhancers could provide a possible solution to this problem [2].

Field-enhanced high-order-harmonic generation (HHG) using plasmonics, generated starting from engineered nanostructures, requires no extra cavities or laser pumping to amplify the pulse power. By exploiting surface plasmon resonances, local electric fields can be enhanced by more than 20 dB [3,4]. This amplification is strong enough to exceed the threshold laser intensity for HHG generation in noble gases and the pulse repetition rate remains unaltered without any extra pumping or cavity attachment. Furthermore, the high-harmonics radiation generated from each nanostructure acts as a pointlike source, enabling collimation or focusing of this coherent radiation by means of (constructive) interference. This opens a wide range of possibilities to spatially arrange nanostructures to enhance or shape spectral and spatial properties in numerous ways.

The basic principle of high-order-harmonic generation based on plasmonics can be summarized as follows (the full explanation can be found in Ref. [2]): a femtosecond low-intensity pulse is coupled to the plasmon mode inducing a collective oscillation of free charges within the metal. The free charges redistribute the electric field around each of the nanostructures, thereby forming a spot of highly enhanced electric field. The enhanced field exceeds the threshold of HHG, thus by injection of noble gases onto the spot of the enhanced field, high order harmonics are generated.

In the seminal experiment of Kim *et al*. [2], the output beam emitted from a modest-power femtosecond oscillator (100 kW peak power, 1.3 nJ pulse energy, 10 fs pulse duration, and 800 nm of wavelength) was directly focused onto a 10×10 μm bowtie nanoantenna array with a pulse intensity of 10^{11} W cm^{-2}, which is about two orders of magnitude less than the threshold intensity to generate HHG in noble gases. Their experimental result showed that the field intensity enhancement factor exceeded 20 dB, which is sufficient to produce XUV wavelengths from the 7th (114 nm) to the 21st (38 nm) harmonics with the injection of xenon gas. Additionally, each bowtie acts as a pointlike source, thus a three-dimensional (3D) arrangement of bowties should enable us to perform control of the generated harmonics in various ways by exploiting interference.

Numerical and semiclassical approaches to study laser-matter processes in atoms and molecules, in particular HHG, are largely based on the assumption that the laser electric field is homogeneous in the region where the electron dynamics takes place [5,6]. Due to the strong confinement of plasmonic hot spots, the laser electric field is clearly no longer homogeneous in the region where the electron dynamics takes place, and consequently important changes in the laser-matter processes would occur. From a theoretical viewpoint, the HHG process can be tackled using different approaches (for a summary, see, e.g., [7,8] and references therein). In this paper, we concentrate our effort on extending two of the most widely used approaches: the numerical solution of the time-dependent Schrödinger equation (TDSE) in reduced dimensions and the strong-field approximation (SFA) [9]. So far, the theoretical work in strong-field physics has been focused on the processes driven by homogeneous coherent electromagnetic radiation on atoms and molecules. Only recently, studies about how HHG spectra are modified due to nonhomogeneous fields, such as those present in the vicinity of a nanostructure irradiated by a short laser pulse, have been published [10,11].

The paper is organized as follows. In Secs. II A and II B, we will present two theoretical approaches to model HHG spectra produced by nonhomogeneous fields, namely, the numerical solution of the time-dependent Schrödinger equation in reduced dimensions (1D-TDSE) and the strong-field approximation (SFA), respectively. We have developed both approaches in such a way as to allow the treatment of very general nonhomogeneous fields, showing the flexibility of both the 1D-TDSE and SFA models. Particular studies of HHG spectra for the simplest case are presented in Sec. III. We will discuss how the nonhomogeneous field produces noticeable modifications in the HHG spectra, namely, a

change in the harmonic periodicity (odd and even harmonics now appear) and a distinct extension in the position of the cutoff (more pronounced for the longer-wavelength cases studied). Both the 1D-TDSE and SFA approaches provide comparable predictions, but by analyzing the HHG process using semiclassical arguments, we can present strong evidence about the motives of the cutoff extension. The paper ends with a short summary and an outlook.

II. THEORY

A. Numerical solution of the time-dependent Schrödinger equation in reduced dimensions (1D-TDSE)

Since the dynamics of an atomic electron in a strong laser field is mainly along the direction of the field (in a linearly polarized laser pulse), it is reasonable to model the HHG in a 1D spatial dimension by solving the following 1D-TDSE:

$$i\frac{\partial\Psi(x,t)}{\partial t} = \mathcal{H}(t)\Psi(x,t) = \left[-\frac{1}{2}\frac{\partial^2}{\partial x^2} + V_{\text{atom}}(x) + V_{\text{laser}}(x,t)\right]\Psi(x,t). \tag{1}$$

To model an atom in 1D, it is common to use the quasi-Coulomb potential,

$$V_{\text{atom}}(x) = -\frac{1}{\sqrt{x^2+1}}, \tag{2}$$

which was first introduced in Ref. [12] and has been widely used in the 1D analysis of an atom. The potential due to the laser electric field linearly polarized along the x axis will be modified in order to treat nonhomogeneous fields. Consequently, we write

$$V_{\text{laser}}(x,t) = E(x,t)x, \tag{3}$$

with

$$E(x,t) = E_0\, f(t)[1+\varepsilon g(x)]\sin\omega t \tag{4}$$

as the laser electric field. In Eq. (4), E_0 is the peak amplitude and ω is the frequency of the coherent electromagnetic radiation. Furthermore, $f(t)$ defines the pulse envelope and ε is a small parameter that characterizes the inhomogeneity region. $g(x)$ represents the functional form of the nonhomogeneities of the electric field (the homogeneous case is $g(x)=0$). In this work, we concentrate our analysis on the simplest form for $g(x)$, i.e., $g(x)=x$, but we should emphasize that the numerical algorithm allows us, in principle, to use any functional form for $g(x)$. We note that for the particular case $g(x)=x$, ε has dimensions of inverse length. To model the laser pulses, we shall use a trapezoidal envelope $f(t)$ given by

$$f(t) = \begin{cases} \frac{t}{t_1} & \text{for } 0 \leqslant t < t_1, \\ 1 & \text{for } t_1 \leqslant t \leqslant t_2, \\ -\frac{(t-t_3)}{(t_3-t_2)} & \text{for } t_2 < t \leqslant t_3, \\ 0 & \text{elsewhere,} \end{cases} \tag{5}$$

where $t_1 = 2\pi n_{\text{on}}/\omega$, $t_2 = t_1 + 2\pi n_p/\omega$, and $t_3 = t_2 + 2\pi n_{\text{off}}/\omega$. Here, n_{on}, n_p, and n_{off} are the number of cycles of turned on, plateau, and turned off, respectively.

The initial state in the 1D-TDSE is the ground state (GS) of the system before we turn on the laser ($t=-\infty$) and it can be found solving an eigenvalue problem once the spatial coordinate x has been discretized. The corresponding eigenvalue for the potential (2) is found to be $\mathcal{E}_{\text{GS}} = -18.2$ eV (-0.67 a.u.). For comparison, we note that the ground-state energy of Ne is -21.6 eV (-0.79 a.u.), and -15.8 eV (-0.58 a.u.) for Ar.

Equation (1) can be solved numerically by using the Crank-Nicolson scheme [5]. In order to avoid spurious reflections from the boundaries, at each time step, the total wave function is multiplied by a mask function of the form $\cos^{1/8}$, which varies from 1 to 0 starting from the 2/3 of the grid [13].

Once the state $\Psi(x,t)$ of the system from the 1D-TDSE (1) is found, we can calculate the harmonic spectrum as follows [14]. The harmonic yield of an atom is proportional to the Fourier transform of the acceleration $a(t)$ of its active electron. That is,

$$D(\omega) = \left|\frac{1}{T_p}\frac{1}{\omega^2}\int_{-\infty}^{\infty} dt e^{-i\omega t} a(t)\right|^2, \tag{6}$$

where T_p is the total duration of the laser pulse. In Eq. (6) $a(t)$ can be obtained by using the commutator relation

$$a(t) = \frac{d^2\langle x\rangle}{dt^2} = -\langle\Psi(t)|[\mathcal{H}(t),[\mathcal{H}(t),x]]|\Psi(t)\rangle, \tag{7}$$

where $\mathcal{H}(t)$ is the Hamiltonian defined in the Eq. (1). The function $D(\omega)$ is called the dipole spectrum, since $D(\omega)$ gives the spectral profile measured in HHG experiments.

B. The strong-field approximation (SFA) for inhomogeneous fields

Another model to evaluate high-harmonic spectra for atoms in intense laser pulses is the Lewenstein model [9]. The main ingredient of this approach is the evaluation of the time-dependent dipole moment $\mathbf{d}(t)$. Within the single active electron (SAE) approximation and considering that the harmonic radiation is directed mainly in the x axis, $\mathbf{d}(t)$ can be written, in the length form [9], as

$$d_x(t) = -i\int_{t_0}^{t} dt' \int d\mathbf{k}\, d_{\text{ion},x}(\mathbf{k}+\mathbf{A}(t'),t') \times d^*_{\text{rec},x}(\mathbf{k}+\mathbf{A}(t))\exp[-iS_0(\mathbf{k},t,t')] + \text{c.c.} \tag{8}$$

In Eq. (8),

$$S_0(\mathbf{k},t,t') = \int_{t'}^{t} dt''\left\{\frac{[\mathbf{k}+\mathbf{A}(t'')]^2}{2} + I_p\right\} \tag{9}$$

is the semiclassical action, I_p is the ionization potential of the atom, and $\mathbf{A}(t) = -\int_{-\infty}^{t}\mathbf{E}(t')dt$ is the vector potential associated with the laser electric field $\mathbf{E}(t)$. The ionization and recombination matrices are given by

$$d_{\text{ion},x}(\mathbf{k},t) = \langle\Psi_{\mathbf{k}}|E(t)\,x|\phi_0\rangle \tag{10}$$

and

$$d_{\text{rec},x}(\mathbf{k}) = \langle\Psi_{\mathbf{k}}|-x|\phi_0\rangle, \tag{11}$$

respectively. Here, $\Psi_{\mathbf{k}}$ is a normalized plane wave of momentum $\mathbf{k}$,

$$\Psi_{\mathbf{k}}(\mathbf{r}) = (2\pi)^{-3/2} e^{i\mathbf{k}\cdot\mathbf{r}}, \tag{12}$$

and ϕ_0 is the undressed initial state of the atom. In our studies, we use normalized hydrogenic $1s$ states of the form

$$\phi_0(\mathbf{r}) = \sqrt{\frac{\lambda^3}{\pi}} e^{-\lambda r}, \tag{13}$$

and we choose the effective charge λ in order to match the energy of the ground state $\mathcal{E}_{\mathrm{GS}}$ of the 1D model atom (see Sec. II A), i.e., $\lambda = \sqrt{2|\mathcal{E}_{\mathrm{GS}}|}$. Using (12) and (13), the explicit expressions for $d_{\mathrm{ion},x}(\mathbf{k})$ and $d_{\mathrm{rec},x}(\mathbf{k})$ are

$$d_{\mathrm{ion},x}(\mathbf{k},t) = i \frac{2^{7/2}\lambda^{5/2}}{\pi} \frac{k_x}{(\mathbf{k}^2+\lambda^2)^3} E(t) \tag{14}$$

and

$$d_{\mathrm{rec},x}(\mathbf{k}) = -i \frac{2^{7/2}\lambda^{5/2}}{\pi} \frac{k_x}{(\mathbf{k}^2+\lambda^2)^3}, \tag{15}$$

respectively. The spectrum of the emitted light polarized along the x axis is obtained by modulus squaring the Fourier transform of the dipole acceleration,

$$a_x(\Omega) = \int_0^{T_p} dt \ddot{d}_x(t) \exp(i\Omega t), \tag{16}$$

where the integration is carried out over the duration of the laser pulse, T_p, by applying a fast Fourier-transform algorithm. The numerical calculation of Eq. (8) involves a multidimensional integration over momentum and time. As usual [9], we have performed the three-dimensional integration over $\mathbf{k}$ using the saddle-point or stationary phase method, meanwhile all time integrations are performed numerically.

Equation (8) has a direct interpretation in terms of the three-step or simple man's model [9]. The first step is the strong-field ionization of the atom or molecule as a consequence of the nonperturbative interaction with the coherent electromagnetic radiation. The classical propagation of the electron in the field defines the second step of the model. Finally, the third step in the sequence occurs when the electron is steered back in the linearly polarized field to its origin, recombining under the emission of a high-energy photon. One of the main features of the HHG process is the coherence of the emitted radiation, which, e.g., opens the possibility of generating attosecond pulses [15].

The Lewenstein model implicitly considers homogeneous electric and vector potential fields, i.e., fields that do not change in the region where the electron dynamics takes place. In order to consider nonhomogeneous fields, the SFA approach needs to be modified accordingly. Our goal is to find the modifications in the electron momentum and the classical action produced by nonhomogeneous fields. The first step is to find the electron trajectories starting from classical arguments employing the Newton equation for an electron moving in a nonhomogeneous electric field $E(x,t)$, linearly polarized in the x axis. It can be then written as

$$\begin{aligned} \ddot{x}(t) &= -\nabla_x V_{\mathrm{laser}}(x,t) = -E(x,t) - [\nabla_x E(x,t)]x \\ &= -E(t)[1 + 2\varepsilon x(t)], \end{aligned} \tag{17}$$

where $V_{\mathrm{laser}}(x,t)$ is given by (3) and we have collected the time-dependent part of the electric field in $E(t)$, i.e., $E(t) = E_0 f(t) \sin\omega t$. We use the Picard iteration [16] extended to the second-order ordinary differential equations to solve Eq. (17), and we restrict ourselves only to the first-order term. The $(n+1)$th-order solution can be written in terms of the nth one as follows:

$$\begin{aligned} X_{n+1}(t) = x_0 + v_0(t-t_0) \\ + \int_{t_0}^{t} \left[\int_{t_0}^{t'} f(t'', X_n(t''), \dot{X}_n(t'')) dt'' \right] dt', \end{aligned} \tag{18}$$

where $x_0 = x(t_0)$, $v_0 = \dot{x}_0 = \dot{x}(t_0)$ and, in our case, $f(t, X_n(t), \dot{X}_n(t)) = -E(t)[1 + 2\varepsilon X_n(t)]$, with $E(t)$ being the time-dependent part of $E(x,t)$, i.e., $E(t) = E_0 f(t) \sin\omega t$. Considering the initial conditions, i.e., $x_0 = 0$ and $v_0 = 0$ (the electron starts its movement at the origin with zero velocity), we finally obtain

$$X_1(t) = \alpha(t) - \alpha(t_0) - A(t_0)(t - t_0), \tag{19}$$

where we have defined $\alpha(t) = \int_0^t dt' A(t')$. The next step is to calculate the classical action and the saddle-point

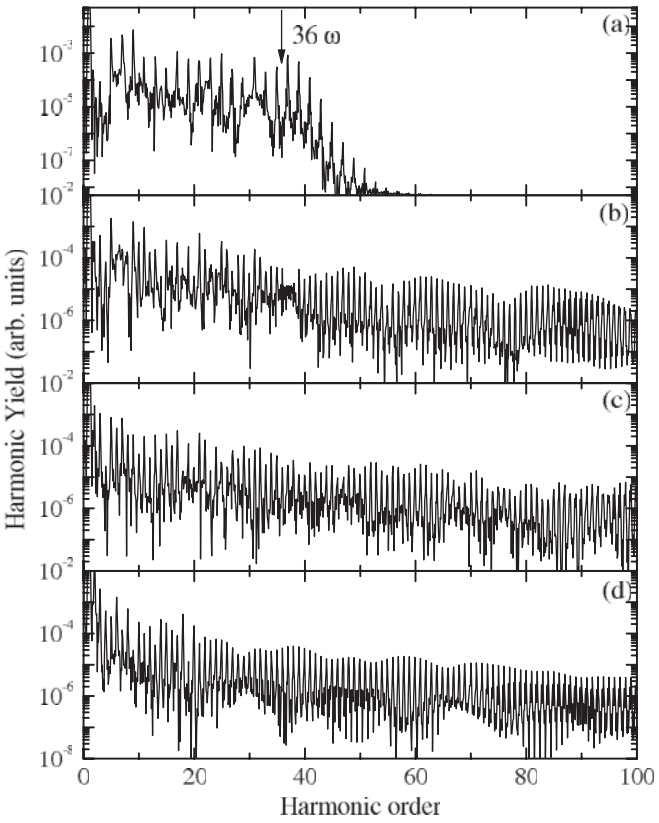

FIG. 1. High-order-harmonic generation (HHG) spectra for a model atom with $\mathcal{E}_{\mathrm{GS}} = -0.67$ a.u. generated using the 1D-TDSE model and with a spatial grid of $x_{\mathrm{lim}} = \pm 7.5\alpha_0$ (see text for details). The laser parameters are $I = 2 \times 10^{14}$ W cm^{-2} and $\lambda = 800$ nm. We have used a trapezoidal-shaped pulse with two optical cycles turned on, i.e., $n_{\mathrm{on}} = 2$, and turned off, i.e., $n_{\mathrm{off}} = 2$, and a plateau with six optical cycles, i.e., $n_p = 6$ (10 optical cycles in total, i.e., approximately 27 fs). The arrow indicates the cutoff predicted by the semiclassical model [9]. (a) Homogeneous case, (b) $\varepsilon = 0.01$ (100 a.u.), (c) $\varepsilon = 0.02$ (50 a.u.), and (d) $\varepsilon = 0.05$ (20 a.u.).

electron momentum starting from the electron trajectories. After elementary algebra, we can write, for the modified action $S(\mathbf{k},t,t')$,

$$S(\mathbf{k},t,t') = S_0(\mathbf{k},t,t') + 2\varepsilon\left[\mathbf{k}\cdot\int_{t'}^{t} dt''\mathbf{A}(t'')X_1(t'') + \int_{t'}^{t} dt''\mathbf{A}^2(t'')X_1(t'')\right], \quad (20)$$

where $S_0(\mathbf{k},t,t')$ is defined in Eq. (9) and $X_1(t)$ is the electron trajectory of Eq. (19). The saddle-point electron momentum is found from the stationary condition

$$\nabla_{\mathbf{k}} S(\mathbf{k},t,t') = 0. \quad (21)$$

Consequently,

$$\nabla_{\mathbf{k}} S(\mathbf{k},t,t') = \nabla_{\mathbf{k}} S_0(\mathbf{k},t,t') + 2\varepsilon\int_{t'}^{t} dt''\mathbf{A}(t'')X_1(t''), \quad (22)$$

with

$$\nabla_{\mathbf{k}} S_0(\mathbf{k},t,t') = \mathbf{k}(t-t') + \alpha(t) - \alpha(t'). \quad (23)$$

Finally, we obtain, for the saddle point or stationary electron momentum $\mathbf{k}_{\rm st}(t,t')$,

$$\mathbf{k}_{\rm st}(t,t') = -\frac{\alpha(t)-\alpha(t')}{(t-t')} - \frac{2\varepsilon}{(t-t')}\int_{t'}^{t} dt''\mathbf{A}(t'')X_1(t''). \quad (24)$$

Replacing (24) in Eq. (20) results in

$$S(\mathbf{k}_s,t,t') = S_0(\mathbf{k}_s,t,t') + 2\varepsilon\left[\mathbf{k}_{\rm st}\cdot\int_{t'}^{t} dt''\mathbf{A}(t'')X_1(t'') + \int_{t'}^{t} dt''\mathbf{A}^2(t'')X_1(t'')\right]. \quad (25)$$

The time-dependent dipole moment, given by Eq. (8), can be written, after the saddle-point method for the momentum $\mathbf{k}$ is applied [9], as

$$d_x(t) = -i\int_{t_0}^{t} dt'\left[\frac{\pi}{\eta + i(t-t')/2}\right]^{3/2} \times d_{{\rm ion},x}(\mathbf{k}_{\rm st}(t,t') + \mathbf{A}(t'),t') \times d^*_{{\rm rec},x}(\mathbf{k}_{\rm st}(t,t') + \mathbf{A}(t))\exp[-iS(\mathbf{k}_{\rm st},t,t')] + \text{c.c.}, \quad (26)$$

where η is a small parameter. We recover the *homogeneous* dipole moment putting $\varepsilon = 0$ in Eq. (26) [9].

III. RESULTS

The results using the 1D-TDSE model developed in Sec. II A are presented in Figs. 1–7. In Figs. 1–6, the laser intensity is $I = 2\times10^{14}$ W cm^{-2} and the laser wavelength is $\lambda =$ 800 nm. We have used a trapezoidal-shaped pulse with two optical cycles turned on, i.e., $n_{\rm on} = 2$, and turned off, i.e., $n_{\rm off} = 2$, and a plateau with six optical cycles, i.e., $n_p = 6$ (10 optical cycles in total, i.e., approximately 27 fs). The model

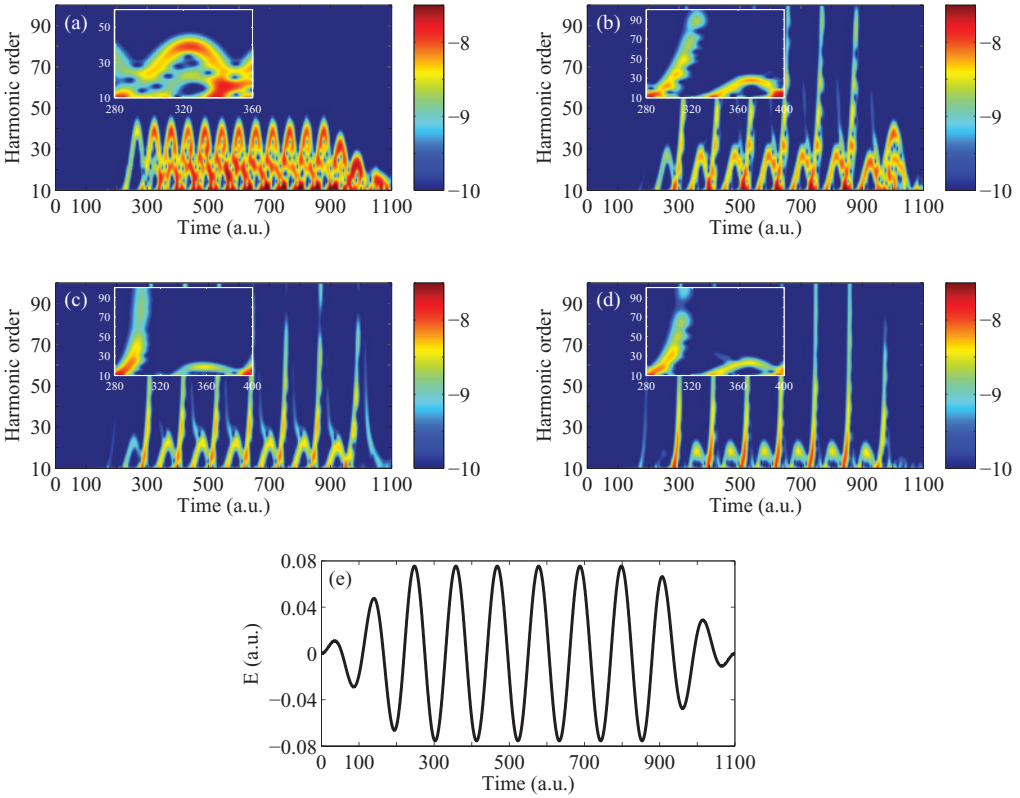

FIG. 2. (Color online) (a)–(d): Gabor analysis for the HHG spectra of Fig. 1. The zoomed regions in all panels show a time interval during the laser pulse for which the complete electron trajectory, from birth time to recollision time, falls within the pulse plateau (see Ref. [17] for details); color scale is logarithmic. (e) Shape of the laser electric field.

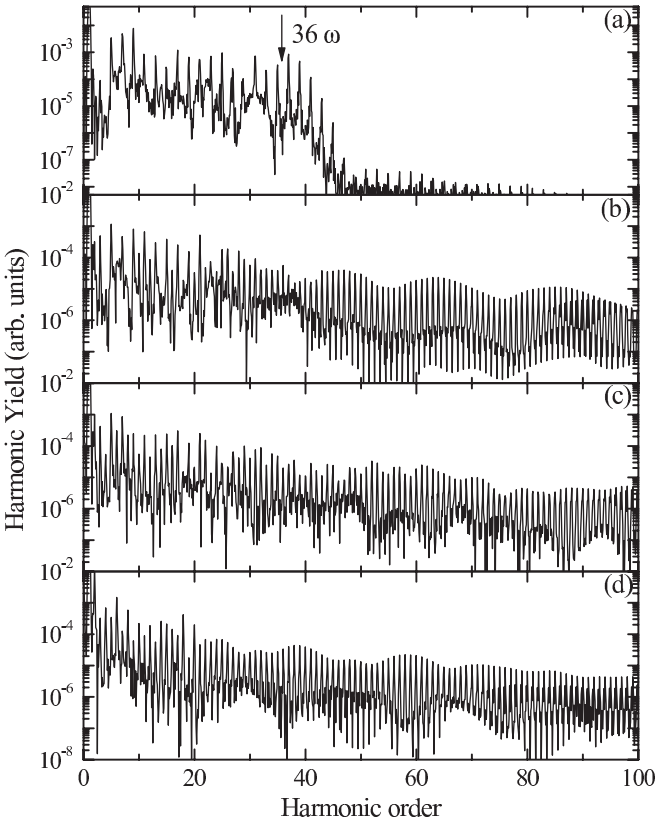

FIG. 3. Same as Fig. 1, but with a spatial grid of $x_{\rm lim} = \pm 4.5\alpha_0$.

atom has $\mathcal{E}_{\rm GS} = -0.67$ a.u. and it is driven by a laser electric field of the form $E(x,t) = E_0 f(t)[1 + \varepsilon x(t)]$, where E_0 is the peak amplitude and $f(t)$ is the pulse envelope [see Fig. 2(e) for a plot of the laser electric field].

One additional parameter we take into account in the 1D-TDSE simulations is the spatial region where the electron moves. This parameter will naturally appear in real situations using bowtie-shaped nanostructures, as those employed in the experiments of Kim *et al.* [2], and when linearly polarized pulses are utilized, which restricts the electron dynamics mostly to one dimension. The bowtie-shaped nanostructures are characterized by a spatial gap that can be, in principle, changed between certain ranges when the nanostructure is engineered. We use, in our 1D-TDSE model, spatial grids in terms of the quiver radius, $\alpha_0 = E_0/\omega^2$, with ω being the driven laser frequency ($\omega = 0.057$ a.u. for a laser wavelength $\lambda = 800$ nm) that in the case under study is $\alpha_0 \approx 23.2$ a.u. (1.23 nm). Three different spatial grid sizes will be employed, namely, $x_{\rm lim} = \pm 7.5\alpha_0$, $x_{\rm lim} = \pm 4.5\alpha_0$, and $x_{\rm lim} = \pm 1.5\alpha_0$, corresponding to gaps of 18.7, 11, and 3.7 nm, respectively.

In Fig. 1, we plot the HHG spectra for different values of ε and for a grid size of $x_{\rm lim} = \pm 7.5\alpha_0$. Figure 1(a) is the homogeneous case, and we have chosen values of 0.01 [Fig. 1(b)], 0.02 [Fig. 1(c)], and 0.05 [Fig. 1(d)] for the inhomogeneity parameter ε that corresponds to inhomogeneity regions of 100 a.u. (5.3 nm), 50 a.u. (2.7 nm), and 20 a.u. (1 nm), respectively. Two distinct characteristics can be observed in Figs. 1(b)–1(d), and we can summarize them as follows: (i) Odd and even harmonics are now present. This new feature appears because we have broken the symmetry of the total potential, $V_{\rm atom} + V_{\rm laser}$, introducing a new asymmetric term, i.e., εx^2; (ii) There is an absence of a clear HHG cutoff. This effect is related to the electron trajectories that contribute to the harmonic spectra and will be the object of study using the Gabor analysis and the semiclassical simulations (see below for details).

Our next step is to use time-analysis tools in order to characterize the HHG spectra calculated using the 1D-TDSE

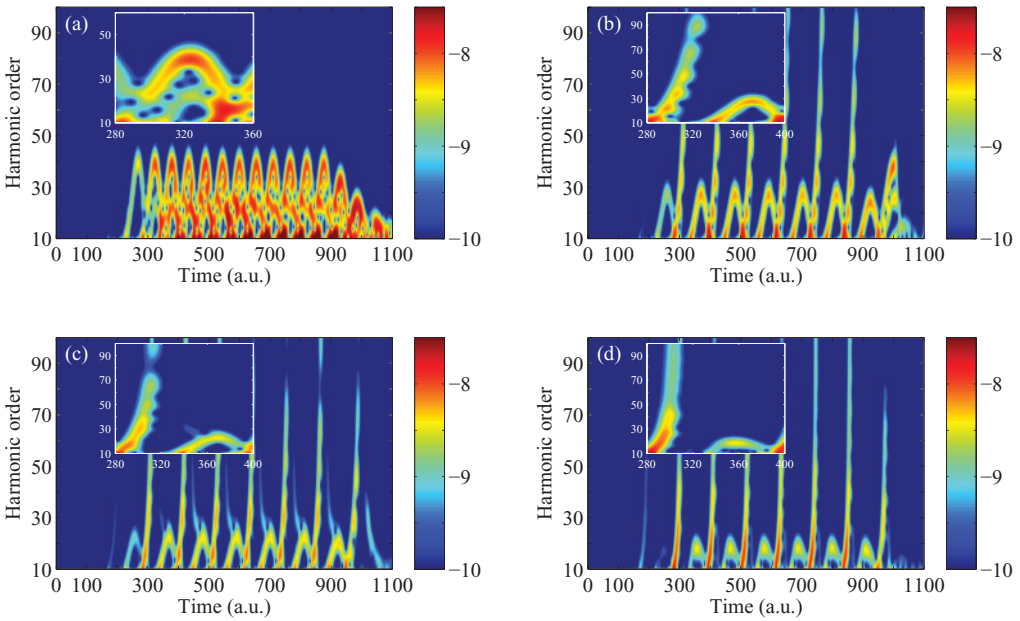

FIG. 4. (Color online) Gabor analysis for the HHG spectra of Fig. 3. The zoomed regions in all panels show a time interval during the laser pulse for which the complete electron trajectory, from birth time to recollision time, falls within the pulse plateau (see text and Ref. [17] for details).

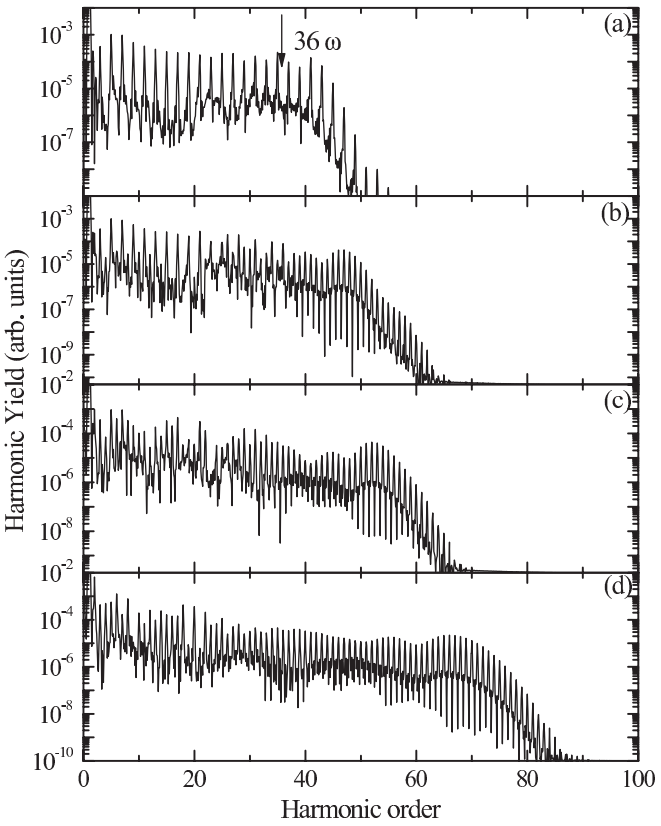

FIG. 5. Same as Fig. 1, but with a spatial grid of $x_{\rm lim} = \pm 1.5\alpha_0$.

model. To this end, we employ the Gabor transformation, developed in the 1940s by Gabor [18], which has proven to be a very powerful tool to estimate the emission times of HHG in atoms and molecules and to discriminate the different electron trajectories [17]. Starting from the dipole acceleration $a(t)$ of Eq. (7), the Gabor transform is defined as

$$a_G(\Omega,t) = \int dt' a(t') \frac{\exp[-(t-t')^2/2\sigma^2]}{\sigma\sqrt{2\pi}} \exp(i\Omega t'), \quad (27)$$

where the integration is usually taken over the pulse duration. In our studies, we use $\sigma = 1/3\omega$, with ω being the central laser frequency. With this value of σ, we achieve an adequate balance between the time and frequency resolutions (see Ref. [17] for details). The results of the Gabor analysis of the HHG spectra of Fig. 1 are presented in Fig. 2. From Figs. 2(a)–2(d) can be observed the clear differences between the homogeneous [Fig. 2(a)] and nonhomogeneous [Figs. 2(b)–2(d)] cases. In the zoomed regions, we show a time interval during the laser pulse for which a complete electron trajectory, from birth time to recollision time, falls within the pulse plateau. From these plots, it is possible to clearly observe the short (for emission times smaller than ∼320 a.u.) and long (the emission times are larger than ∼320 a.u. for this case) trajectories (see Ref. [17] for more details). The highest harmonic order (around the 40th) is generated at an emission time of ∼320 a.u. for the homogeneous case. On the other hand, only an *extended* short trajectory (with emission times smaller than ∼320 a.u.) is present for all of the nonhomogeneous cases, and no clear harmonic cutoff is visible.

Alternatively, in Figs. 3 and 4, we plot the HHG spectra for different values of ε and the Gabor analysis, respectively. Here a grid size of $x_{\rm lim} = \pm 4.5\alpha_0$ is used. Figures 3(a) and 4(a) are the homogeneous case and we have chosen values of 0.01 [Figs. 3(b) and 4(b)], 0.02 [Figs. 3(c) and 4(c)], and 0.05 [Figs. 3(d) and 4(d)] for the inhomogeneity parameter ε that corresponds to inhomogeneity regions of 100 a.u. (5.3 nm), 50 a.u. (2.7 nm), and 20 a.u. (1 nm), respectively. We note that the difference between these last two figures (Figs. 3 and 4) and

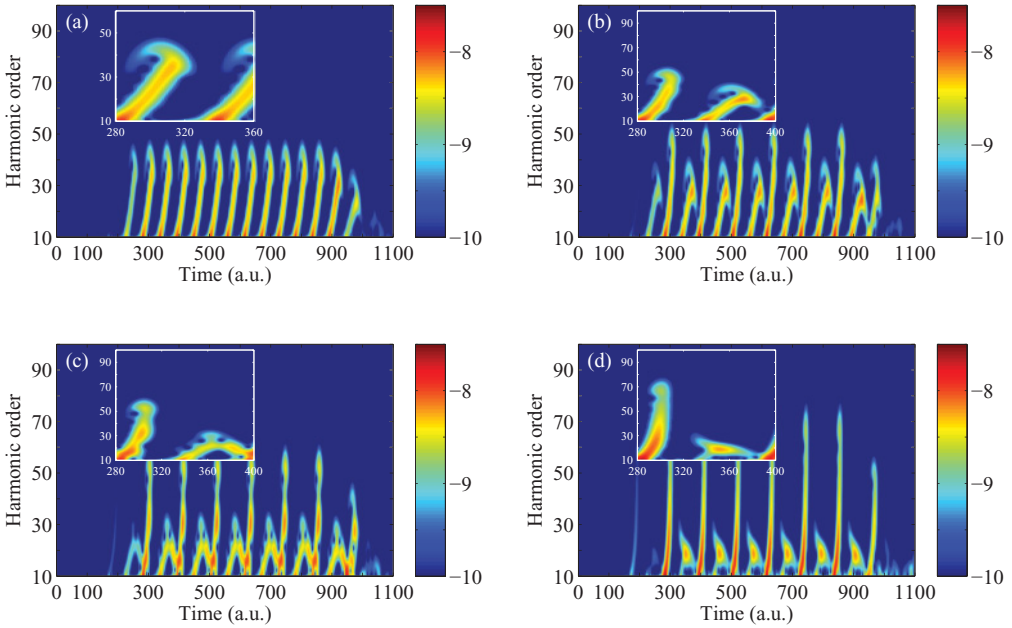

FIG. 6. (Color online) Gabor analysis for the HHG spectra of Fig. 5. The zoomed regions in all panels show a time interval during the laser pulse for which the complete electron trajectory, from birth time to recollision time, falls within the pulse plateau (see text and Ref. [17] for details).

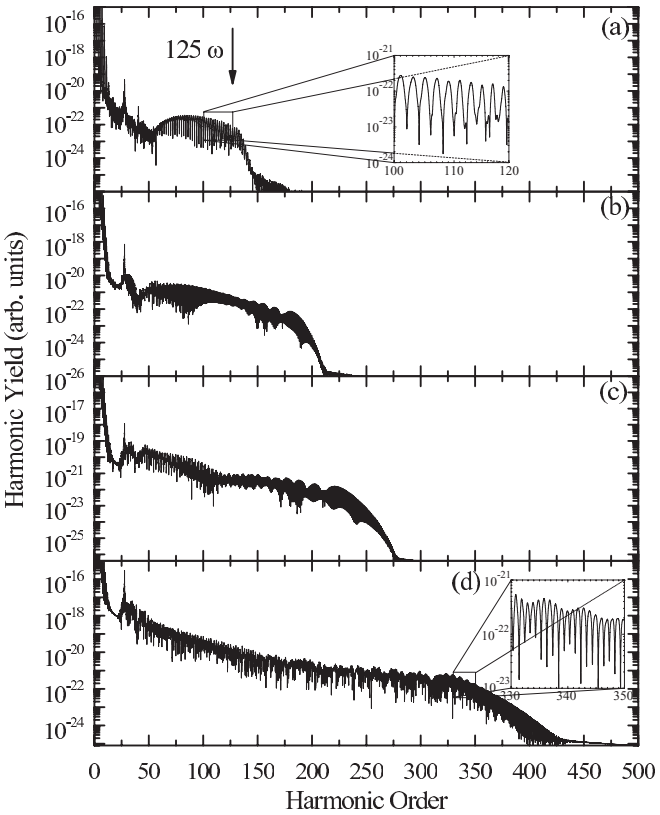

FIG. 7. HHG spectra for a model atom with $\mathcal{E}_{GS} = -0.67$ a.u. generated using the 1D-TDSE model and with a spatial grid of $x_{lim} = \pm 1.5\alpha_0$ (see text for details). The laser parameters are $I = 1 \times 10^{13}$ W cm^{-2} and $\lambda = 3.2$ μm (3200 nm). We have used a Gaussian-shaped pulse with six cycles FWHM. The arrow indicates the cutoff predicted by the semiclassical model [9] and the zoomed regions correspond to harmonic order values between (a) 100 and 120 ω, and (d) 330 and 350 ω, respectively (see text for further details).

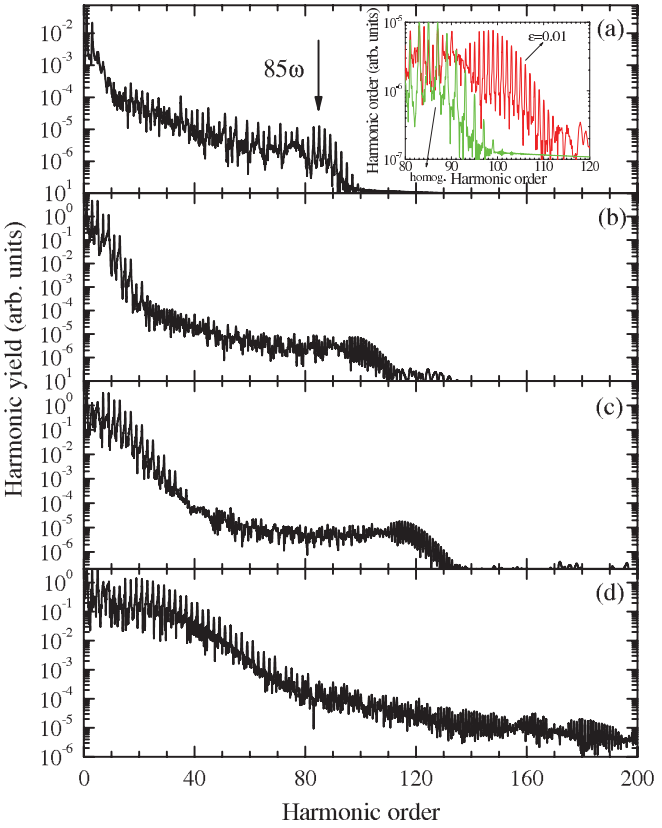

FIG. 8. (Color online) HHG spectra for a model atom with $\mathcal{E}_{GS} = -0.67$ a.u. generated using the extended SFA approach. The laser parameters are $I = 6 \times 10^{14}$ W cm^{-2} and $\lambda = 800$ nm. We have used a trapezoidal-shaped pulse with three optical cycles turned on and turned off, and a plateau of four constant-amplitude optical cycles [see Fig. 9(e)]. The arrow indicates the cutoff predicted by the semiclassical model [9]. (a) Homogeneous case, (b) $2\varepsilon = 0.01$ (100 a.u.), (c) $2\varepsilon = 0.02$ (50 a.u.), and (d) $2\varepsilon = 0.05$ (20 a.u.). The inset in panel (a) shows a particular zoomed region for the harmonic spectra of (a) and (b) near the cutoff region (see the text for details).

Figs. 1 and 2 is hardly visible for all of the cases, showing that the decrease of the grid size has no effect in the HHG spectra, both for the homogeneous and nonhomogeneous cases.

Finally, in Figs. 5 and 6, we plot the HHG spectra for different values of ε and the Gabor analysis, respectively, and now with a grid size of $x_{lim} = \pm 1.5\alpha_0$. Figures 5(a) and 6(a) are the homogeneous case and we have chosen values of 0.01 [Figs. 5(b) and 6(b)], 0.02 [Figs. 5(c) and 6(c)], and 0.05 [Figs. 5(d) and 6(d)] for the inhomogeneity parameter ε that corresponds to inhomogeneity regions of 100 a.u. (5.3 nm), 50 a.u. (2.7 nm), and 20 a.u. (1 nm), respectively. Here it is possible to observe the substantial differences between the results shown in Figs. 5(b)–5(d) and 6(b)–6(d) and those from panels (b)–(d) of Figs. 1–4, showing that the electron confinement, jointly with the inhomogeneities of the laser electric field, are responsible for the appearance of a clearly extended harmonic cutoff. We also note that the HHG spectra for the homogeneous case [Figs. 1(a), 3(a), and 5(a)] are identical for all of the cases, confirming that the electron confinement is not the only responsible for the distinct features present in the HHG spectra. In some sense, when we restrict the electron movement, only the short trajectories contribute to the formation of the harmonic spectrum, and this feature is clearly visible in the zoomed regions of the Gabor analysis in Fig. 6, where only short trajectories are distinguishable, i.e., those with emission times smaller than ∼320 a.u.

In order to explore how our 1D-TDSE approach behaves, we have calculated HHG spectra for longer wavelengths. We present our results in Fig. 7 for $\lambda = 3.2$ μm. This value for λ represents an example that could be perfectly reachable experimentally [19,20] and allow us to reach numbers for the electron excursion region (i.e., the quiver radius α_0) closer to those considered in real experiments [2]. The laser intensity is $I = 1 \times 10^{13}$ W cm^{-2}, and we have employed a Gaussian-shaped pulse with six cycles FWHM, $f(t) = \exp[-\frac{2\ln 2}{\tau^2}t^2]$, where τ is the FWHM (full width at half maximum) duration of the driving laser intensity $I(t)$ ($\propto |E(t)|^2$). We use a spatial grid of $x_{lim} = \pm 1.5\alpha_0$, where $\alpha_0 = 83$ a.u. (4.4 nm), i.e., the electron dynamics is confined in a region of around 13.2 nm. The panels correspond to the homogeneous case [Fig. 7(a)], $\varepsilon = 0.01$ [Fig. 7(b)], $\varepsilon = 0.02$ [Fig. 7(c)], and $\varepsilon = 0.05$ [Fig. 7(d)], respectively. We have included zoomed panels for the cases of Figs. 7(a) and 7(d). These two plots allow us to observe clearly the presence of odd and even harmonics

for this particular nonhomogeneous case [Fig. 7(d)], and only the appearance of odd harmonics for the homogeneous one [Fig. 7(a)]. From Fig. 7, we conclude that for longer wavelengths, the cutoff extension due to the nonhomogeneities of the field, combined with the electron confinement, is far more pronounced, e.g., for the case of $\lambda = 3.2$ μm and $\varepsilon = 0.05$, the cutoff is almost three times larger than the homogeneous case. This extension could open the avenue for the production of attosecond pulses in the keV regime (for a theoretical study at $\lambda = 800$ nm, see [11]). Furthermore, the region of confinement using these laser parameters is closer to values that could be found in real nanostructures.

In the following, we use the modified SFA model presented in the Sec. II B to generate HHG spectra produced by nonhomogeneous fields. We employ a laser pulse with an electric field of the form $E(x,t) = E_0 f(t)[1 + 2\varepsilon x(t)]$, where E_0 is the peak amplitude, $f(t)$ is the pulse envelope, and we use only the first order for $x(t)$, i.e., $x(t) \approx X_1(t)$ with $X_1(t)$ of (19). In Fig. 8, we show the predictions of this model, and Fig. 9 represents the Gabor analysis of the HHG spectra of the former. In order to enhance the new HHG features and see more clearly the differences between the studied cases, the laser field now has an intensity of $I = 6 \times 10^{14}$ W cm^{-2} and a wavelength of $\lambda = 800$ nm. We have used a trapezoidal-shaped pulse with three optical cycles turned on ($n_{\text{on}} = 3$) and turned off ($n_{\text{off}} = 4$), and a plateau of four constant-amplitude optical cycles ($n_p = 4$) [see Fig. 9(e)] and the model atom has $\mathcal{E}_{\text{GS}} = -0.67$ a.u. With these parameters, the predicted cutoff is $n_c = 85$, as is shown by the arrow plotted in Fig. 8(a). Furthermore, Figs. 8(b)–8(d) correspond to values of $2\varepsilon = 0.01$, $2\varepsilon = 0.02$ and $2\varepsilon = 0.05$, respectively. As in the case of the 1D-TDSE model, the SFA approach predicts the appearance of odd and even harmonics and a cutoff extension. In order to show these features more clearly, we have zoomed out a small region of the HHG near the cutoff for Figs. 8(a) and 8(b). In this graph, it is more transparent to see how the inhomogeneous fields modify the harmonic spectra. An additional feature appears and it could be extracted from Figs. 8(a) (homogeneous case) and 8(d) ($2\varepsilon = 0.05$): there exists a clear enhancement in the harmonic yield in the plateau region (see, e.g., a region around the 25th–40th harmonics). The Gabor analysis of the HHG spectra calculated using the SFA, shown in Fig. 9, shows similarities and differences between this model and the 1D-TDSE approach (the SFA approach does not account for the restrictions on the electron motion). For example, in Fig. 9(c), only short trajectories appear to contribute to the HHG spectra (similar to the $x_{\text{lim}} = \pm 1.5\alpha_0$ case); meanwhile, Fig. 9(d) has analogous features to Figs. 2(d) and 4(d) (i.e., the $x_{\text{lim}} = \pm 7.5\alpha_0$ and $x_{\text{lim}} = \pm 4.5\alpha_0$ cases, respectively). This behavior could be related to the limited validity of the perturbation-like character of the SFA approach developed in Sec. II B. An extension of the SFA approach including the quantum orbits analysis will be presented elsewhere.

We now concentrate our efforts in order to explain, using the semiclassical three-step model, the extension of the harmonic

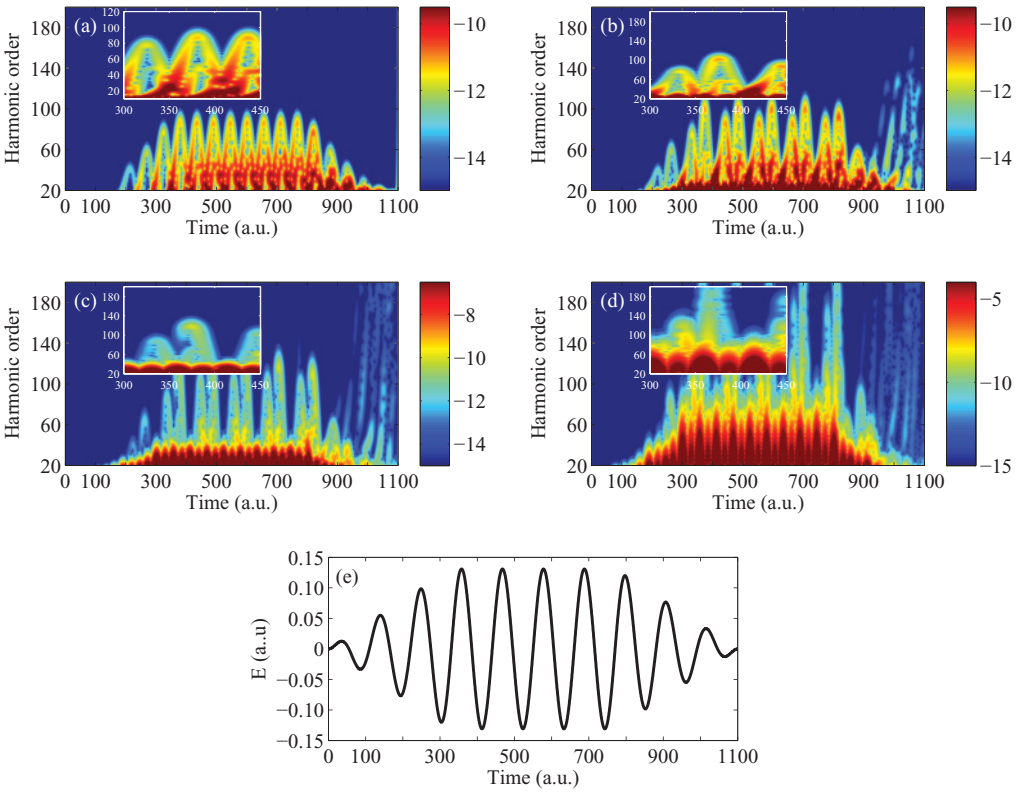

FIG. 9. (Color online) (a)–(d): Gabor analysis for the HHG spectra of Fig. 8. The zoomed regions in all panels show a time interval during the laser pulse for which the complete electron trajectory, from birth time to recollision time, falls within the pulse plateau (see text and Ref. [17] for details); color scale is logarithmic. (e) Shape of the laser electric field.

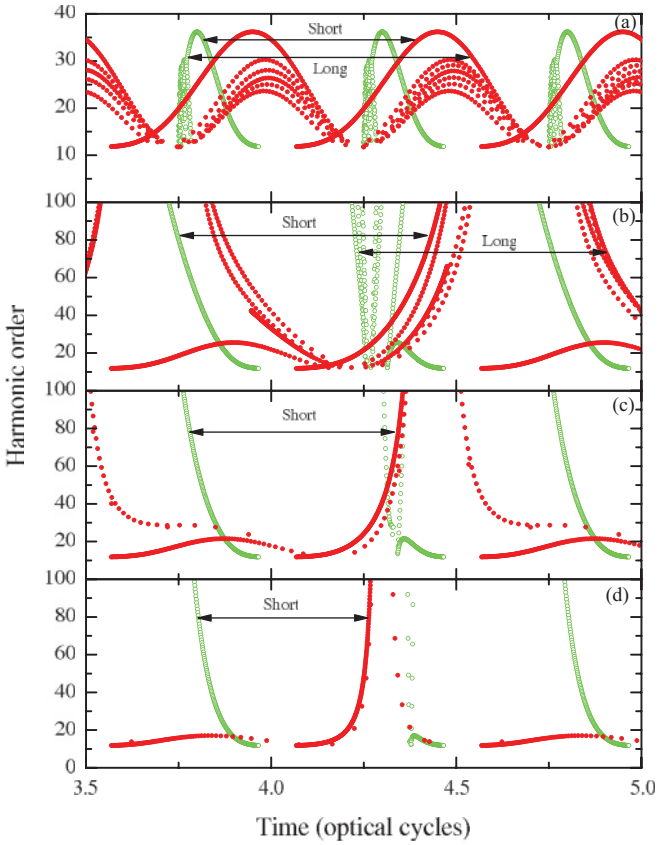

FIG. 10. (Color online) Total energy of the free electron (in terms of the harmonic order) in the laser field when it recollides with its parent ion obtained from Newton's second law and plotted as a function of the ionization time (green open circles) or the recollision time (red filled circles). (a) Homogeneous case, (b) $\varepsilon = 0.01$ (100 a.u.), (c) $\varepsilon = 0.02$ (50 a.u.), and (d) $\varepsilon = 0.05$ (20 a.u.). In all cases, the motion of the electron is not restricted.

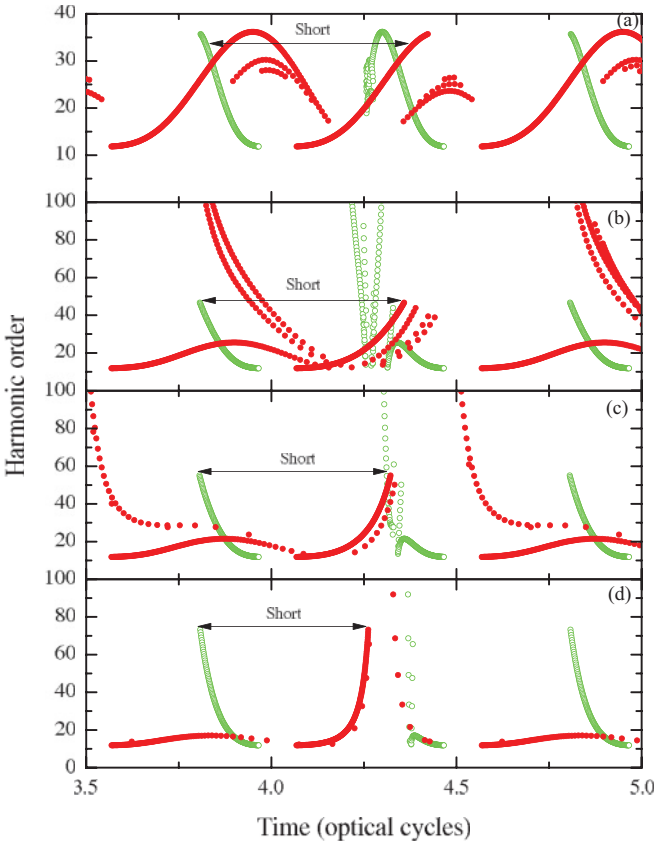

FIG. 11. (Color online) Same as Fig. 10, but with the motion of the electron confined into a region $[-\alpha_0, +\alpha_0]$.

cutoff. As was already pointed out, this new feature appears as a consequence of the combination of two factors, namely, the nonhomogeneous character of the laser electric field and the confinement in the electron motion. It is well known that the position of the HHG cutoff holds

$$n_c\omega = 3.17U_p + I_p, \tag{28}$$

where n_c is the harmonic order at the cutoff, ω is the laser frequency, U_p is the ponderomotive energy ($U_p = I/4\omega^2$, with I being the laser intensity in a.u.), and I_p is the ionization potential of the atom or molecule [9]. This relationship can be obtained solving the classical Newton equation for an electron moving in a linearly polarized electric oscillating field under the following conditions (the resulting model is also known as the simple man's model): (i) the electron starts with zero velocity at position zero at time $t = t_0$ (t_0 is known as ionization time), i.e., $x(t_0) = 0$ and $\dot{x}(t_0) = 0$ for our 1D model; (ii) when the electric field reverses its direction, the electron returns to its initial position (i.e., *recollides* with its parent ion) at a later time, $t = t_1$ (t_1 is also known as recollision time), i.e., $x(t_1) = 0$. The electron kinetic energy at the return time t_1 can be obtained from $E_k(t_1) = \dot{x}(t_1)^2/2$, and, finding the value of t_1 (as a function of t_0) that maximizes this energy, Eq. (28) is fulfilled.

We have solved numerically the Newton equation for an electron moving in a linearly polarized (in the x axis) electric field with the same parameters used in the 1D-TDSE calculations. Specifically, we find the numerical solution of $\ddot{x}(t) = -\nabla_x V_{\text{laser}}(x,t)$ with $V_{\text{laser}}(x,t)$ given by (3), and $E(x,t)$ of Eqs. (4) and (5) without any approximation, i.e., we solve Eq. (17). For fixed values of ionization time t_0, it is possible to compute the classical trajectories and to numerically calculate the times t_1 where the electron recollides, i.e., $x(t_1) = 0$. Also, once the ionization time t_0 is fixed, the electron trajectory is completely determined. In Figs. 10(a)–10(d), we plot the dependence of the harmonic order on the ionization time (t_0) and recollision time (t_1), calculated from $n = [E_k(t_i) + I_p]/\omega$, with $i = 0$ and $i = 1$, and for the cases presented in the 1D-TDSE simulations, i.e., homogeneous [Fig. 10(a)], $\varepsilon = 0.01$ [Fig. 10(b)], $\varepsilon = 0.02$ [Fig. 10(c)], and $\varepsilon = 0.05$ [Fig. 10(d)], respectively. At this point, we have not restricted the electron trajectories, and consequently we allow the electron to move in all of the space (see below for details). The temporal axis, i.e., the x axis, is plotted in terms of optical cycles and we have chosen a *temporal* window from 3.5 to 5 optical cycles (i.e., from 380 to 550 a.u.). In all of the panels of Fig. 10, both the short and long trajectories (see, e.g., [11]) are labeled. From Fig. 10(a), it is possible to observe that the maximum kinetic energy of the returning electron is in perfect agreement with Eq. (28) (no harmonic order beyond $n_c \sim 36$ is reached). On the other hand, Figs. 10(b)–10(d) show how the nonhomogeneous field modifies the electron trajectories and

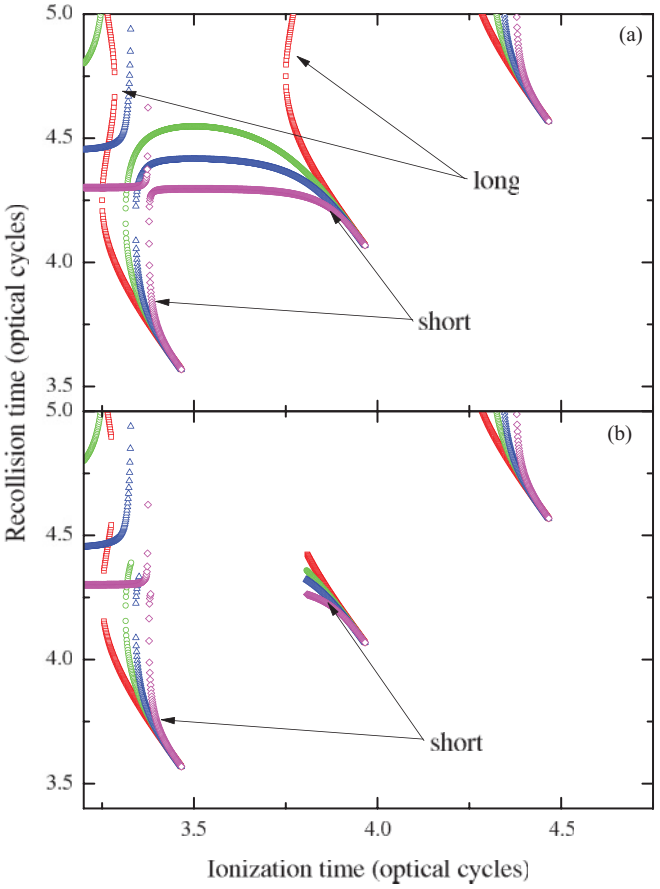

FIG. 12. (Color online) Dependence of the semiclassical trajectories on the ionization and recollision times for different values of ϵ and for (a) the nonconfined case and (b) the confined case. Red squares are homogeneous case $\varepsilon = 0$; green circles are $\varepsilon = 0.01$; blue triangles are $\varepsilon = 0.02$, and magenta diamonds are $\varepsilon = 0.05$.

that no clear HHG cutoff is observed. This is consistent with the predictions of the 1D-TDSE for the largest spatial grids [see Figs. (2) and (4)]. Although from Figs. 10(b)–10(d) we observe no clear HHG cutoff, the kinetic energy gained by the electron is finite in agreement with the energy conservation. Furthermore, Figs. 10(b)–10(d) show similar features as those observed in Figs. 2(b)–2(d) and 4(b)–4(d), i.e., only *extended* short trajectories contribute to the harmonic radiation. This characteristic is related with the modifications the electron trajectories suffer due to the nonhomogeneities of the field (see below for details).

In order to classically simulate the 1D-TDSE results, but for the smallest grid size, i.e., $x_{\rm lim} = \pm 1.5\alpha_0$, we restrict the classical electron trajectories to the domain $[-\alpha_0,\alpha_0]$. The $\pm\alpha_0$ values represent the starting point of the mask function and consequently a fair comparison is possible. The results are presented in Figs. 11(a)–11(d). From these plots, we can argue that only short trajectories contribute to the harmonic radiation. This is related to the electron motion restriction, i.e., the *confinement*, which we have now incorporated in the classical simulations. Furthermore, a clear HHG cutoff is now observed for all of the nonhomogeneous cases and its value is in clear agreement with the 1D-TDSE predictions [see Figs. 5(b)–5(d) and 6(b)–6(d)].

Finally, in Fig. 12, the recollision time t_1 of the electron is presented as a function of the ionization time t_0 and for several values of ε. Figure 12(a) represents the nonconfined case and, in Fig. 12(b), we have restricted the electron motion into the region $[-\alpha_0,\alpha_0]$. The long trajectories are those with recollision times $t_1 \gtrsim 4.25$ optical cycles and, only for the homogeneous case (red squares in figure), these trajectories are clearly visible. On the other hand, short trajectories are characterized by $t_1 \lesssim 4.25$ optical cycles and these are present for both the homogeneous and nonhomogeneous cases. Our results are consistent with those shown in Ref. [11], but note our inhomogeneity parameter is more than one order of magnitude higher. From Fig. 12(a), we observe how the long trajectories are modified by the nonhomogeneity, namely, the *homogeneous* long trajectories (red squares) with ionization times t_0 around the 3.25 and 3.75 optical cycles *merge* into unique trajectories. Additionally, the branch with $t_0 \sim 3.75$ now has ionization times more than half an optical cycle smaller when ε increases; hence, the times spent by the electron in the continuum increase. This fact explains the vanishing long trajectories seen in Figs. 10(b)–10(d). Additionally, the electric field strength at the ionization time for short trajectories is higher than for long trajectories, and, considering the ionization rate as a highly nonlinear function of this electric field [21,22], long trajectories are much less efficient than the short ones. On the other hand, short trajectories are almost independent of ε and only for higher values are noticeable differences visible. When the electron motion is confined, shown in Fig. 12(b), only short trajectories are present for all of the cases and this confirms the fact that long trajectories are absent and only the short trajectories contribute to the formation of the harmonic radiation.

IV. CONCLUSIONS AND OUTLOOK

We studied high-order-harmonic generation in a model atom produced by nonhomogeneous fields. These fields are not merely a theoretical speculation but are present in a vicinity of a metal nanostructure when it is irradiated by a short laser pulse. We have extended two of the most widely used models, namely, the numerical solution of the time-dependent Schrödinger equation (TDSE) in reduced dimensions and the semiclassical approach known as strong-field approximation (SFA). Both models are able to predict the new features that appear due to the presence of inhomogeneities, namely, the appearance of odd and even harmonics and an extension in the cutoff position. The latter feature is a consequence of the combination of the nonhomogeneous electric field and the confinement of the electron dynamics, as can be extracted from the Gabor analysis and the semiclassical simulations made for all of the studied cases. We have proven the robustness of the 1D-TDSE model using different laser parameters, and by solving the classical equation of motion for an electron moving in a linearly polarized nonhomogeneous electric field, we are able to understand the reasons for the cutoff extension.

The models presented allow one to use, in principle, any functional form for the nonhomogeneous fields. Moreover, they are able to incorporate real parameters in the simulations, such as the region dimensions where the electron dynamics takes place. We plan to continue our investigations in this

direction, jointly with studies of other laser-matter processes driven now by these nonhomogeneous fields.

ACKNOWLEDGMENTS

We acknowledge the financial support of the MINCIN projects (FIS2008-00784 TOQATA and Consolider Ingenio 2010 QOIT) (M.F.C. and M.L.); ERC Advanced Grant QUAGATUA, the Alexander von Humboldt Foundation, and Hamburg Theory Prize (M.L.); Spanish Ministry of Education and Science through its Consolider Program Science (SAUUL CSD 2007-00013), Plan Nacional (Grant No. FIS2008-06368-C02-01), and LASERLAB-EUROPE (Grant Agreement No. 228334, EC's Seventh Framework Programme) (J.B.). This research has been partially supported by Fundació Privada Cellex. Useful and enlightening discussions with Manfred Lein are gratefully acknowledged. M.F.C. acknowledges Mitsuko Korobkin and Dane Austin for help and advice in the numerical implementation of the 1D-TDSE model.

[1] F. Krausz and M. Ivanov, Rev. Mod. Phys. **81**, 163 (2009).
[2] S. Kim, J. Jin, Y.-J. Kim, I.-Y. Park, Y. Kim, and S.-W. Kim, Nature (London) **453**, 757 (2008).
[3] P. Mühlschlegel, H.-J. Eisler, O. J. F. Martin, B. Hecht, and D. W. Pohl, Science **308**, 1607 (2005).
[4] P. J. Schuck, D. P. Fromm, A. Sundaramurthy, G. S. Kino, and W. E. Moerner, Phys. Rev. Lett. **94**, 017402 (2005).
[5] M. Protopapas, C. H. Keitel, and P. L. Knight, Rep. Prog. Phys. **60**, 389 (1997).
[6] T. Brabec and F. Krausz, Rev. Mod. Phys. **72**, 545 (2000).
[7] P. Sailères, A. L'Huillier, P. Antoine, and M. Lewenstein, in *Advances of Atomic and Molecular Physics*, edited by B. Bederson and H. Walther (Academic, New York, 1999).
[8] M. Lewenstein and A. L'Hullier, in *Strong Field Laser Physics*, edited by T. Brabec, Springer Series in Optical Sciences, Vol. 134 (Springer, Berlin, 2008).
[9] M. Lewenstein, P. Balcou, M. Y. Ivanov, A. L. Huillier, and P. B. Corkum, Phys. Rev. A **49**, 2117 (1994).
[10] A. Husakou, S.-J. Im, and J. Herrmann, Phys. Rev. A **83**, 043839 (2011).
[11] I. Yavuz, E. A. Bleda, Z. Altun, and T. Topcu, Phys. Rev. A **85**, 013416 (2012).
[12] Q. Su and J. H. Eberly, Phys. Rev. A **44**, 5997 (1991).
[13] J. L. Krause, K. J. Schafer, and K. C. Kulander, Phys. Rev. A **45**, 4998 (1992).
[14] K. J. Schafer and K. C. Kulander, Phys. Rev. Lett. **78**, 638 (1997).
[15] P. B. Corkum and F. Krausz, Nature Phys. **3**, 381 (2007).
[16] C. H. Edwards and D. E. Penney, *Differential Equations and Boundary Value Problems–Computing and Modeling*, 4th ed. (Prentice Hall, Englewood Cliffs, NJ, 1999).
[17] C. C. Chirila, I. Dreissigacker, E. V. van der Zwan, and M. Lein, Phys. Rev. A **81**, 033412 (2010).
[18] D. Gabor, J. Inst. Electr. Eng. **93**, 429 (1946).
[19] A. Thai, M. Hemmer, P. Bates, O. Chalus, and J. Biegert, Opt. Lett. **36**, 3918 (2011).
[20] J. Biegert, O. Chalus, and P. Bates, IEEE J. Sel. Top. Quantum Electron. **18**, 531 (2012).
[21] L. V. Keldysh, JETP **47**, 1945 (1964) [Sov. Phys. **20**, 1307 (1965)].
[22] M. V. Ammosov, N. B. Delone, and V. P. Krainov, Sov. Phys. JETP **64**, 1191 (1986).